CHAPTER 2 – LITERATURE REVIEW

The performance of drilled shafts with anomalies requires an understanding of the design of drilled shafts without anomalies and then the impact of anomalies on the structural and geotechnical capacities. This study focuses on the effects of anomalies on the drilled shaft capacity under axial load. This chapter includes a comprehensive review of the effects of anomalies on drilled shaft capacity, design methods for drilled shaft axial capacity, and load transfer curves for drilled shaft axial capacity computation.

2.1 LITERATURE REVIEW OF CAPACITY OF DRILLED SHAFTS WITH ANOMALIES

A literature review on shafts with anomalies revealed that the studies were all recent. The following is a brief discussion from these existing studies.

Petek, et al. (2002), studied the effect of anomalies on drilled shaft axial capacity using the finite element program, PLAXIS. The drilled shafts were modeled as two-dimensional with weak layer and neck-in type anomalies in three different cohesive soil profiles. The soil properties used in analyses were modified to fit the test results. The anomalies were located at different depths within the shaft, near the top, at the middle, and near the bottom. The rectangular-shaped neck-in anomalies produced the greatest effect on drilled shaft capacity. The weak layer anomaly was modeled by low quality concrete. The study also found that the anomalies in the drilled shafts in strong soils imposed a greater effect on the drilled shaft capacity than those in weaker soils. The results showed that the effect of anomalies is dependant on their locations within the shaft. The anomalies located near the top have more effect on the drilled shaft capacity than those located at the middle and near the bottom.

Iskander, et al. (2003), studied drilled shafts constructed with anomalies located in various areas within the shaft as shown in Figures 2, 3, and 4. The purpose of the study was to assess the effect of anomalies on the axial capacity of drilled shafts in varved clay. Six drilled shafts were installed with spacing greater than five times the shaft diameter. A 1-m diameter shaft was augured to a depth of approximately 6 m with a temporary protective steel casing, and a 0.9-m diameter shaft was then augured to the final depth of 14.3 m without slurry. The reinforcing steel cage with 10 #9 steel and #4 stirrups were installed before concrete placement. Four, 52-mm inside diameter, steel pipes were installed in all shafts except for Shaft #3, which had only three pipes for the cross-hole sonic logging to study the effect of tube on test results. Concrete with 28-day strength of 28 kPa was placed using both the free fall and tremie-tube methods.

The shafts were numbered from #1 through #6, and shafts #2 and #6 were constructed with no built-in anomalies. Shafts #1, #3, #4, and #5 were constructed with built-in anomalies representing necking, voids, caving soils, and soft bottoms. The anomalies were made of a variety of materials, and some anomalies were filled with in situ soils to replicate inclusions on side walls as shown in Figures 3 and 4. The void size varies from 5 to 11% of the cross-sectional area and 0.3 to 1.5 m in length. Soil inclusions vary from 5 to 17% of the cross-sectional area. Necking was built into the shaft using 100 mm corrugated flexible plastic tubing; the occupancy

of necks was approximately 45% of the cross-sectional area and 10% for external necks. None of the shaft bottoms were cleaned but appeared to be clean prior to concrete placement. The shafts were tested using various NDT testers, with the results show in Figures 3 and 4.

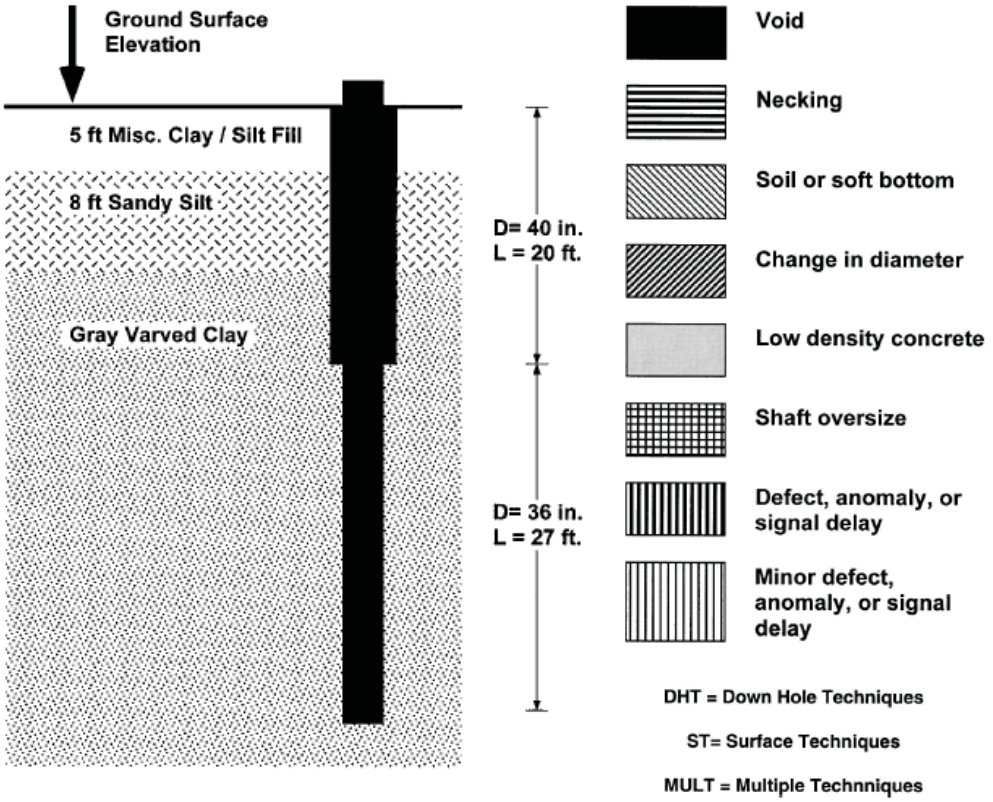

Figure 2. Drilled shaft profile in varved clay and legend for planned and predicted anomalies (Iskander, et al., 2003).

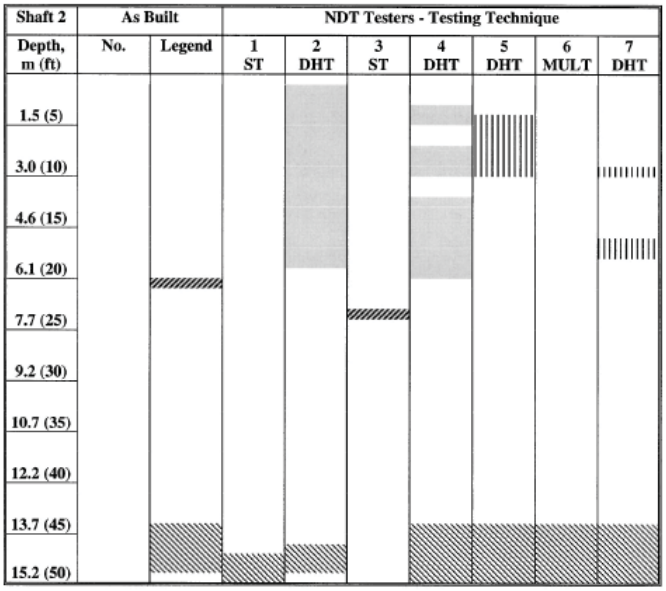

Figure 3. Planned and predicted anomalies in Shaft #2 (Iskander, et al., 2003).

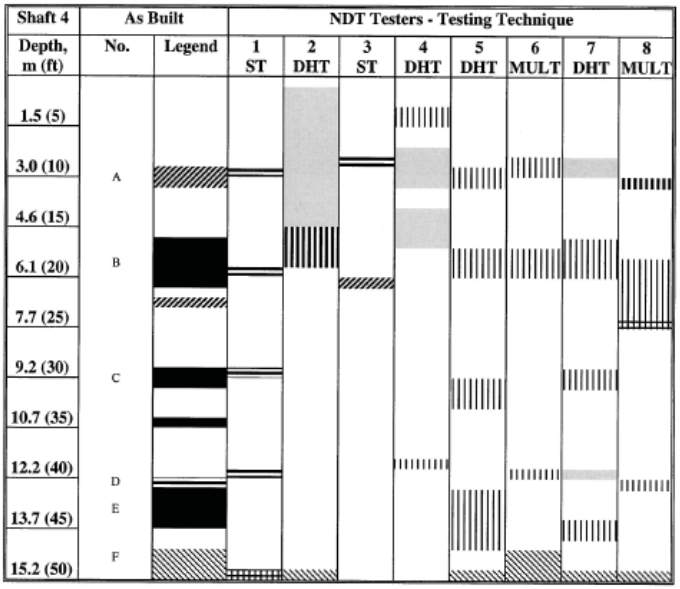

Figure 4. Planned and predicted anomalies in Shaft #4 (Iskander, et al., 2003)

Load tests on Shaft #2, which was 1.2 m shorter than the other shafts, with no planned structural anomalies and soft bottom and Shaft #4 with planned structural anomalies as shown in Figure 4, and sound bottom were performed. Both shafts were loaded to reach failure load in which Shaft #4 was loaded twice. The comparison of the capacity of two shafts is shown in Table 1. The cohesion-bearing capacity factor for the end bearing capacity of both shafts was assumed to be equal to 9, and the mobilized undrained shear strength of clay was back calculated.

Table 1. The comparison capacity of Shafts #2 and #4.

Shaft #	Davisson's Failure Criteria (kN)	Load Test Capacity (kN)	Load Test End Bearing Capacity (kN)	Undrained Shear Strength at Shaft Base (kPa)
2	1000	1200	≤200	34.0
4 (loading)	950	1060	300	51.0
4 (reloading)	880	1000	250	42.5

The capacity of the drilled shaft with no planned structural anomalies but with soft bottom was 5% to 10% higher than the shaft with a sound bottom and some structural anomalies. The increase of strength was insignificant, so the difference between the two drilled shafts was not recorded during construction. The mobilized undrained shear strength of 34 kPa at Shaft #2 with soft bottom was 33% lower than the virgin end bearing one at Shaft #4.

O'Neill, et al. (2003), studied the effect of undetectable structural flaws on the axial and lateral capacity of drilled shafts. Eleven scaled drilled shaft samples were tested in the lab to study the structural behavior of reinforced concrete drilled shafts with minor flaws under flexural and axial

compression loadings. Tests were performed to determine the effects of 1) shape and size of voids on the shaft's structural capacity, 2) stress concentration near the void location, 3) buckling of longitudinal reinforcement in compression within the void, and 4) strength of variations of defective shafts.

All of the shaft specimens were about one-third scale of a real shaft with 305 mm diameter; 2,260 mm length for the laterally loaded tests; and 1,830 mm length for the axially loaded tests. The specimens were tested under three different loadings: pure flexural, pure axial compression, and combined flexural and axial compression. Areas of reinforcement in specimens were 2.12% with No. 4, Grade 60, $f_y = 414$ MPa steel bars arranged in equal space around the perimeter. The smooth wire spirals with 25.8 mm^2 of the cross-sectional area, $f_y = 448$ MPa are spaced at 25.4 mm. The concrete cover around the case was 25.4 mm. Figure 5 shows the two shapes of voids (Type 1 and Type 3), which closely simulate voids typically observed in real shafts. The voids were 15% of the gross cross-sectional area of the specimens. In all tests, voids were located in the middle on the compression side of the specimens.

Concrete cylinder tests showed that the 28-day strength of concrete, f_c', varies from 41.3 to 45.9 MPa. In flexural tests, behaviors of defective specimens and perfect specimens are similar before yielding of reinforcement. The void significantly affected the reinforcement strength after yielding, and the Type 2 void shape imposed a more significant effect than the Type 1 void shape. The effect of void length is insignificant on strength and ductility. Failure criterion of flexural tests was chosen at a mid-span deflection of 40 mm, equivalent to concrete strain of 0.003 on top of most specimens. The moment capacity reductions of Type 1 and Type 2 specimens were about 16.5% and 33%, respectively. In axial compression tests, Figure 6 shows that voids significantly affected the shaft capacity, especially for the Type 2 void, mainly due to the lack of concrete confinement and reinforcement buckling. The axial compressive strengths were reduced by 3.5% and 7.2% for a Type 1 void with lengths of 153 mm and 305 mm, respectively, and 8.3% for a Type 2 void. The analytical strengths using ACI 318 and AASHTO Bridge Design Specification for spirally reinforced concrete under pure axial compression are 9% higher than the test results. For the combined loading test, before the yielding of reinforcement, the stiffness of the intact shaft specimen was lightly greater than the defective shaft one. Both capacity and ductility reductions are significant for the Type 2 void as shown in Figure 7. O'Neill, et al., indicated that their analytical results differed from test results by 17% due to the limitations of their computational methods attributed to the omission of factors, including strain hardening of steel, the buckling of steel rebar in the presence of a void, the longitudinal length of the void, the effect of transverse steel and the void on concrete confinement, the stress concentration in the void, and the potential steel-concrete debonding.

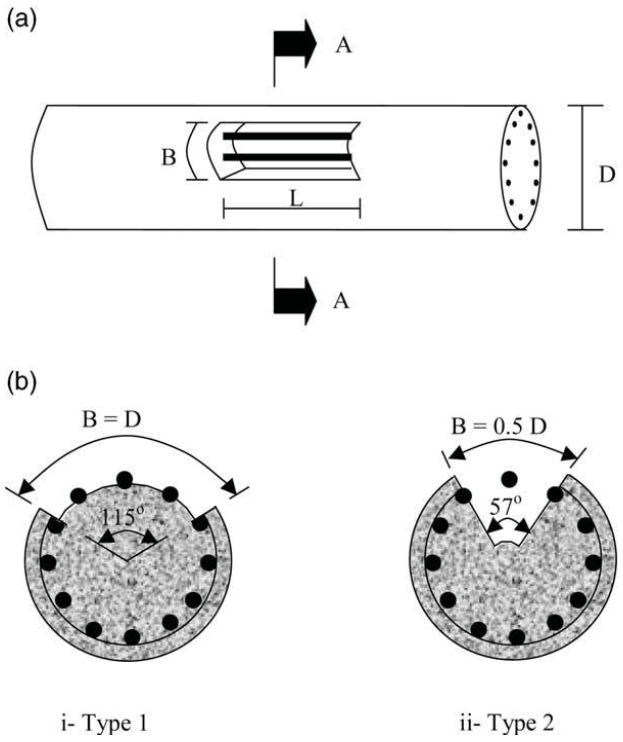

Figure 5. Parameter of void flaws: a) three dimension view; b) Section A-A (after O'Neill, et al., 2003).

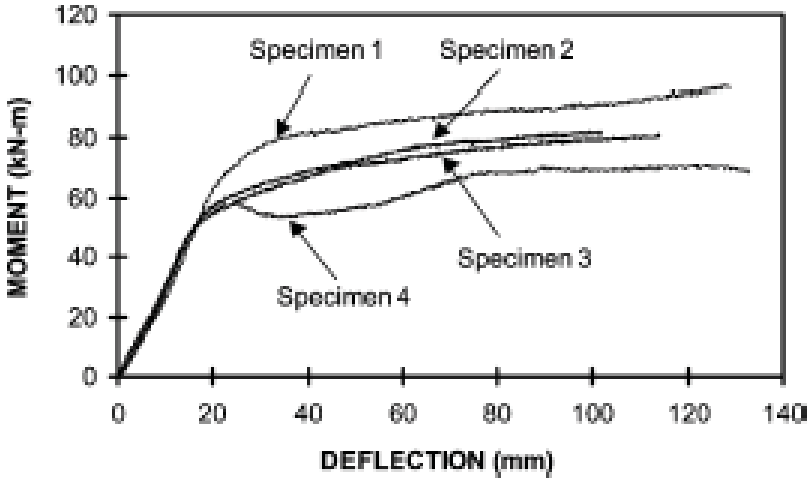

Figure 6. Moment deflection curves for flexural tests (after O'Neill, et al., 2003).

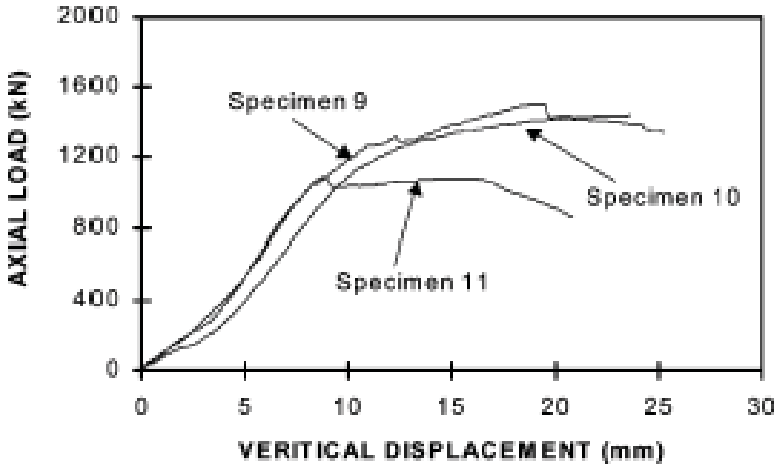

Figure 7. Moment deflection curves for combined loading tests (after O'Neill, et al., 2003).

Mullins and Ashmawy (2005) reported the findings of an experimental study on factors affecting anomaly formation in drilled shafts. The most interesting finding was that, even at the most frequently specified rebar clear spacing to aggregate diameter ratio of 3 to 5, a substantial build-up of material inside the cage was observed before enough pressure was developed to push concrete mix through the reinforcing cage into the annular region outside the cage. This allows the formation of anomalies in the annular area outside the cage. The rate of concreting was also observed to significantly affect the anomaly formation in the annular region of the drilled shaft outside the cage.

Jung G., et al. (2006), evaluated the effect of anomalies in drilled shafts on capacity. Four full-scale drilled shafts with artificial anomalies and one sound drilled shaft were constructed and tested. The artificial anomalies included soft bottom, concrete segregation, honeycomb, and contractions of cross sections by 10% to 20% as shown in Figure 8, respectively. During the static load test, load-settlement curves and load transfer curves were recorded. The numerical analyses using the finite difference program, FLAC 3D were performed to simulate the axial resistance behavior of drilled shafts.

From the analyses, the load-settlement and load transfer curves of drilled Shaft #4 with 10% contraction anomalies and Shaft #5 with 20% contraction anomalies were in good agreement with the test results. In comparison to the same curves of drilled shafts with anomalies of 10% to 20% cross section contraction, there was little difference. The measured values of normalized axial stress in each drilled shaft were both less than those of numerical analyses. For drilled Shaft #4, the difference was 7%; and, for drilled Shaft #5, the difference was 30% as shown in Figure 9.

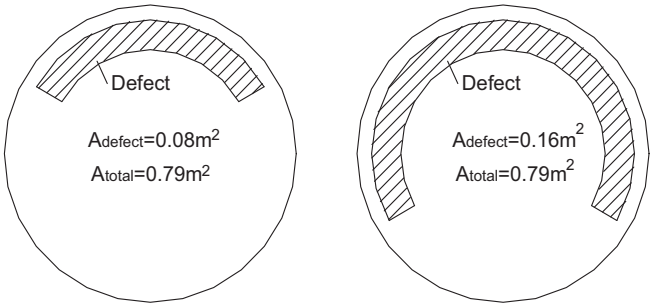

Figure 8. Asymmetric anomaly (Jung, et al., 2006).

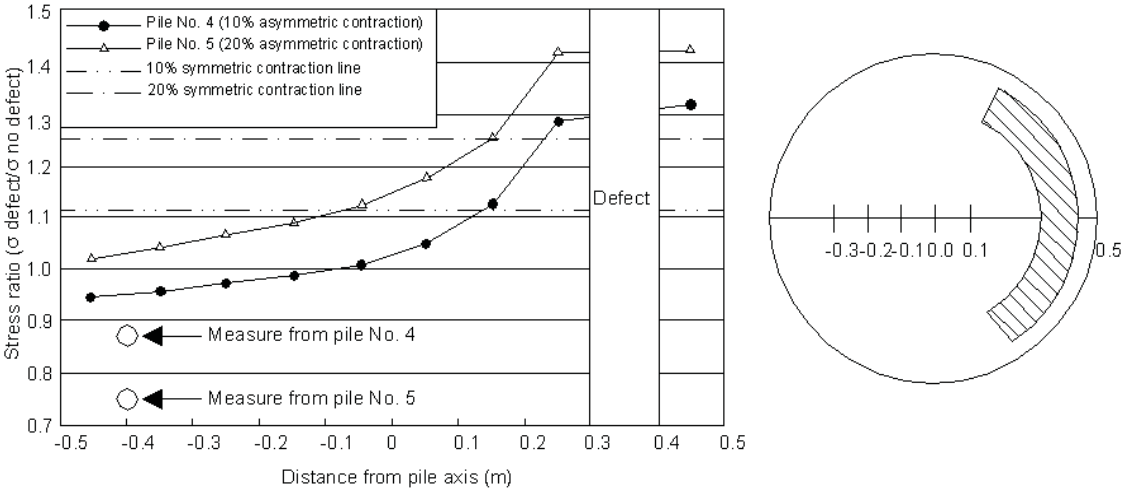

Figure 9. Normalized axial stress across defective section (Jung, et al., 2006).

Haramy (2006) presented a timely comprehensive study on the performance monitor of concrete mix during its hydration process, CSL detection of anomaly locations, tomographic imaging of the anomaly, and the effects of anomalies on drilled shaft capacity. Subsequently, two articles (Haramy, et al., 2007a and b) were published in the proceedings of the DFI 32nd Annual Conference on the related topics. Quality assurance and quality control of drilled shafts has become a concern due to difficulties in accurately locating construction anomalies, such as shown in Figure 9, and determining load bearing capacity of defected drilled shafts. Various non-destructive evaluation techniques have been developed to estimate the integrity of the concrete in drilled shafts. While these techniques have been widely accepted, variables and unknowns can affect the measurement results. Results are typically difficult to interpret, leading to unnecessary construction delays and possible litigation over shaft integrity. In addition, influences of surrounding ground materials, stress states under different load conditions, and crack and residual stress development during concrete hydration further complicate determination of shaft performance.

Figure 10. Typical cylindrical anomaly in a drilled shaft (Haramy, 2006).

Haramy, et al. (2007a), showed that 1) the curing environment could greatly affect the concrete strength and required close monitoring during construction; and 2) the NDE technology could effectively monitor curing temperature, density, and moisture, which could significantly affect the velocity measured in the cross-hole sonic logging, the rate of strength gain, and the final strength of concrete in drilled shafts and, thereby, affect their structure capacities. To understand the mechanism by which a drilled shaft cures under field conditions, three newly constructed drilled shafts were monitored for up to 7 days, immediately following concrete placement. The shaft curing rate was found to vary with depth, shaft diameter, surrounding geo-material types, and the depth of groundwater.

CSL logging showed that the sonic velocity increased with curing time until 4 to 7 days; and, at a specific time, the velocity appeared to be inversely correlated to curing temperatures. The gamma-gamma density log (GDL) showed that the average density increased with curing time but decreased slightly in 3 to 5 days. At a given time the GDL density curves seemed to correlate with the neutron moisture logging (NML) curve. The moisture was highest when surrounded by bedrock, then clay, then sand due to different hydration rates. It was found that NDE monitoring was effective in monitoring concrete curing temperature, density, velocity, and moisture; the concrete curing strength in drilled shafts is a function of time, thermal conductivity, the permeability of the surrounding soil/rock, and the depth of groundwater table.

Haramy, et al. (2007b), focused on the evaluation of load bearing capacity of drilled shafts with anomalies under various conditions by 3-D numerical analysis and modeling to evaluate the serviceability of a defected drilled shaft. Study results showed that friction angles of

surrounding geo-materials, soil density, and percentage of consolidation influence the stress concentration around anomalies and that such stress concentration can trigger crack propagation and worsen the corrosion process. When anomalies occur, the NDE methods can assist in detecting their locations and sizes. The anomaly near the top of a drilled shaft will significantly affect the structural capacity of drilled shafts. When lacking concrete confinement for reinforcement, the effect of an anomaly on a drilled shaft is more significant because of the potential for buckling.

In summary, while much research has been done on the subject of the effect of anomalies on a drilled shaft's behavior, none has comprehensively studied the effect of anomalies on a drilled shaft's capacity in different geomaterial environments, which this study aims to examine. To effectively study the subject matter, an effective computational program is needed. **PSI-VA** (**Pile-Soil i**nteraction program for **v**ertical loaded drilled shafts with **anomalies**) was used. Some characteristics of PSI-VA are presented in Chapters 3 and 4, and the analysis results are presented in the subsequently chapters.

2.2 DESIGN METHOD FOR AXIAL CAPACITY

2.2.1 Design for axial capacity in cohesive soil

2.2.1.1 Side resistance in cohesive soils

The following equation gives the α method for the evaluation of the skin (side or frictional) resistance of drilled shafts in cohesive soils at depth z:

$$f_s = \alpha c_u \qquad \text{(Eq. 1)}$$

where

f_s = ultimate skin resistance at depth z

c_u = undrained shear strength (cohesion) at depth z

α = empirical adhesion factor dependant upon undrained cohesion.

Kulhawy and Jackson (1989) reported 65 uplift and 41 compression field tests of drilled shafts and obtained the values of α area as shown in Figure 11. The values of α varies from 0.3 to 1.0. The following best-fit functional relationship (Eq. 2) shows that the α values decrease with the increasing undrained shear strength:

$$\alpha = 0.21 + 0.25\frac{p_a}{c_u} \qquad \text{(Eq. 2)}$$

where p_a = atmospheric pressure. In other words, the soft, normally consolidated clay has a higher α value than the hard, overconsolidated clay.

O'Neill and Reese (1999) collected data from many case histories to develop a correlation between c_u and f_s.

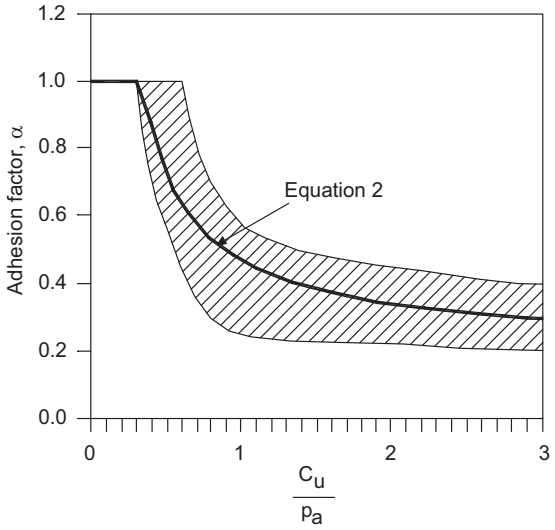

Figure 11. Variation of α with c_u/p_a (Kulhawy and Jackson, 1989).

The database was based on shafts in clay with $c_u \geq 50$ kPa and the following drilled shaft dimensions of $0.7 \leq D \leq 1.83$ m, $L \geq 7$ m. O'Neill and Reese (1999) recommended the following equation for the average value of α:

$$\alpha = 0.55 \qquad \text{for } \frac{c_u}{p_a} \leq 1.5 \qquad \text{(Eq. 3)}$$

and

$$\alpha = 0.55 - 0.1\left(\frac{c_u}{p_a} - 1.5\right) \qquad \text{for } 1.5 \leq \frac{c_u}{p_a} \leq 2.5 \qquad \text{(Eq. 4)}$$

For the case of $c_u/p_a > 2.5$, skin resistance should be calculated as the method for cohesive intermediate geomaterials (O'Neill and Reese, 1999). If the shaft length from ground surface to a depth of about 1.5 m is excluded in calculating shaft resistance to account for soil shrinkage in the zone of seasonal moisture change, then $\alpha = 0$ at depth $z \leq 1.5$ m. The lower part of the drilled shaft is also excluded because, in compression loads, the displacement of the soil at the shaft tip will generate tensile stresses in the soil that will be relieved by cracking of soil; and pore water suction will be relieved by inward movement of groundwater (O'Neill and Reese, 1999). If the length of this portion is equal to D above the shaft base, then $\alpha = 0$ at depth $z \geq L - D$.

The total skin resistance, Q_s, is equal to the peripheral area of the shaft multiplied by the unit side resistance shown as follows:

$$Q_s = \pi D \sum \alpha^i c_u^i L^i \qquad \text{(Eq. 5)}$$

where D = shaft diameter; L^i = thickness of layer i; and where the values of α and c_u are constants.

2.2.1.2 End bearing in cohesive soils

The prediction of end bearing capacity of drilled shafts in clays is much less uncertain than is the prediction of skin resistance (Reese, et al., 2006). The equation below is used for calculating the net base resistance, Q_p:

$$Q_p = A_p c_u N_c^* \qquad \text{(Eq. 6)}$$

where A_p = the area of the base; c_u = an average undrained shear strength of clay calculated over a depth of two times the diameter below the base (Reese, et al., 2006); and N_c^* = the bearing capacity factor (usually taken to be 9) when the ratio L/D_b is ≥ 4 (Das, 1999). According to O'Neill and Reese (1999), for the straight shaft the full value of $N_c^* = 9$ is obtained when the base movement is about 20% of D. If the base movement is unknown, the bearing capacity factor N_c^* can be calculated by (Reese, et al., 2006):

$$N_c^* = 1.33\left(\ln I_r + 1\right) \qquad \text{(Eq. 7)}$$

where I_r is the rigidity index of saturated clay under undrained condition:

$$I_r = \frac{E_s}{3c_u} \qquad \text{(Eq. 8)}$$

where E_s is undrained Young's modulus. If E_s is not measured, N_c^* and I_r can be estimated from Table 2.

Table 2. Values of I_r and N_c^* (Reese, et al., 2006).

c_u	$E_s/3c_u$	N_c^*
24 kPa (500 lb/ft^2)	50	6.5
48 kPa (1000 lb/ft^2)	150	8.0
≥ 96 (2000 lb/ft^2)	250-300	9.0

2.2.2 Design for axial capacity in cohesionless soil

2.2.2.1 Skin resistance in cohesionless soil

Meyerhoff (1976) gives the unit skin resistance based on an SPT test:

$$f_s = \frac{N}{100} \text{ (tsf)} \qquad \text{(Eq. 9)}$$

where N is the average SPT value, not corrected for overburden pressure.

The following equation is used to calculate the ultimate unit skin resistance in sand at depth z :

$$f_{sz} = K\sigma'_z \tan\delta \qquad \text{(Eq. 10)}$$

where K = a parameter that includes the effect of the lateral pressure coefficient and a correlation factor; σ'_z = the vertical effective stress in soil at depth z; and δ = the friction angle at the interface of the shaft surface and soil.

The total side resistance calculated from the summation of each layer of the unit side resistance multiplied by the perimeter and the layer thickness is shown as follows:

$$Q_s = \pi D \sum K^i \sigma_z'^i \tan\varphi_c^i L_i \qquad \text{(Eq. 11)}$$

Kulhawy (1991) suggested that the value of the interface friction angle, δ, was smaller than the soil friction angle, φ, and was affected by construction. For drilled shafts, δ/φ is equal to 1.0 for good construction techniques and 0.8 or smaller with poor slurry construction (Rollin, et al., 2005). The coefficient of lateral pressure, K, is a function of the coefficient of lateral pressure at rest, K_0, and the stress changes caused by construction, loading, and desiccation. The analysis of field load tests shows that the value of K ranges from 0.1 to over 5.0 and the K/K_0 ratio varies from 0.67 to 1.0 (Rollin, et al., 2005).

O'Neill and Reese (1999) suggested the expression for the ultimate unit skin resistance in sand:

$$f_{sz} = \beta\sigma'_z \le 200 \text{ kPa} \qquad \text{(Eq. 12)}$$

and

$$Q_s = \pi D \sum \beta^i \sigma_z'^i L_i \qquad \text{(Eq. 13)}$$

where

in sands use
$\beta = 1.5 - 0.245z^{0.5}$; ($0.25 \le \beta \le 1.20$) for SPT $N_{60} \ge 15$ B/0.3 m or
$\beta = \left(N_{60}/15\right)\left(1.5 - 0.245z^{0.5}\right)$ for SPT $N_{60} < 15$ B/0.3 m.

in gravelly sands or gravels, use the method for sands if $N_{60} < 15$ B/0.3 m (O'Neill and Reese, 1999).

Rollins, et al. (2005), studied a total of 28 axial tension (uplift) tests performed at eight different sites in Northern Utah to determine the values of K and β for gravelly sand and gravel. The back-calculated K values varied with depth as shown in Figure 12, where the values of lateral earth pressure at rest $(K_0)_{NC}$ and Rankine passive pressure coefficient K_p for a range of friction angles are also shown. The back-calculated K values reach K_p near the ground surface and decrease to $(K_0)_{NC}$ at some depth. The high K values observed could be caused by the increase in lateral pressure during shearing due to dilation of granular soils. Near the ground surface with low confining pressure, the soil would dilate during shearing, causing a significant increase in lateral pressure. At greater depth, the increase in lateral pressure is less severe because of reduced chance of dilation under a higher confining (or overburden) pressure. From the above observations and other references, Rollins, et al. (2005), concluded that it may be inappropriate to determine K based on the normal stress prior to the test. The back-calculated β values from the tests both from and outside Utah are plotted in Figure 13. The data point scatter might be due to the differences in gradation, particle angularity, fines content, geologic age, OCR, and construction methods. The mean curve for gravels is significantly greater than the mean curve for gravelly sand, and both curves show the k values greater than those values from the design curve for sand from O'Neill and Reese (1999). The equations for evaluation of β values for gravelly sands and gravels are summarized in Table 3.

Table 3. β for Gravelly sands and gravels (Rollins, et al., 2005).

Percentage Gravel	β
Less than 25%	$\beta = 1.5 - 0.135z^{0.5}$; $0.25 \le \beta \le 1.20$
Between 25% and 50%	$\beta = 2.0 - 0.0615z^{0.75}$; $0.25 \le \beta \le 1.80$
Greater than 50%	$\beta = 3.4e^{-0.0265z}$; $0.25 \le \beta \le 3.0$

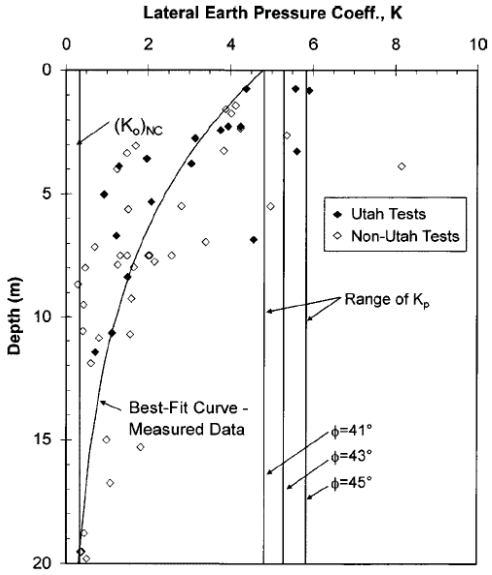

Figure 12. Back-calculated lateral earth pressure coefficient K versus depth for load tests along with boundaries for $(K_0)_{NC}$ and K_p (Rollins, et al., 2005).

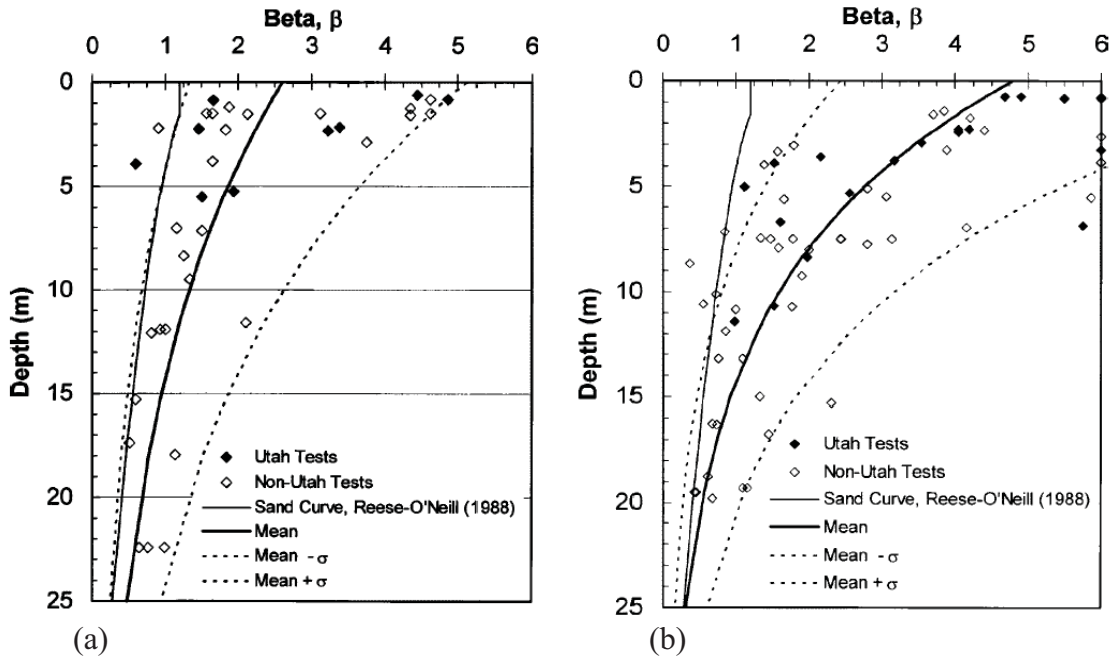

Figure 13. Back-calculated β versus depth from load tests in (a) gravelly sands and (b) gravels along with best fit curves and the curves for the upper and lower bound curves with plus and minus one standard deviation σ (Rollins, et al., 2005).

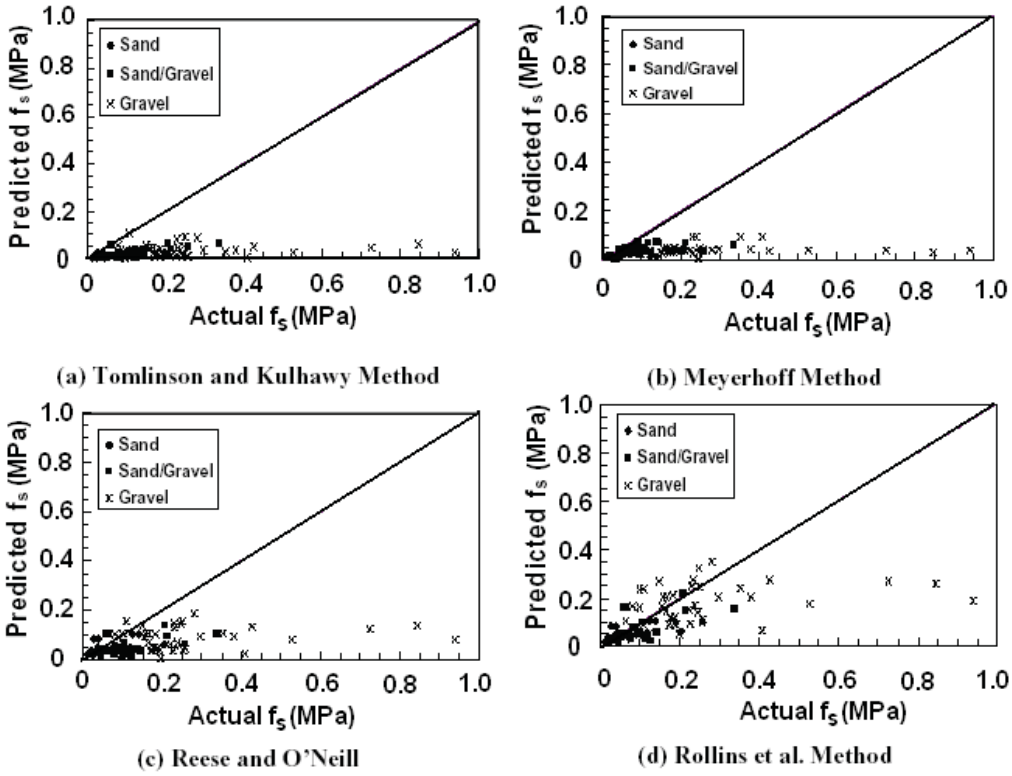

Figure 14. Predicted and actual f_s values for sands, sandy gravels, and gravels (Harraz, et al., 2005).

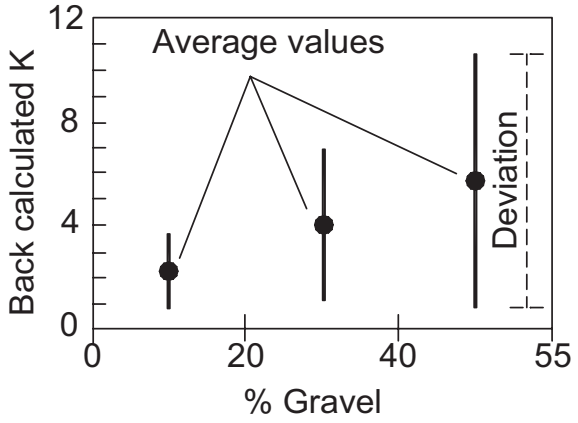

Figure 15. Back-calculated Horizontal stress to Vertical stress ratio, K, vs. % Gravel (Harraz, et al., 2005).

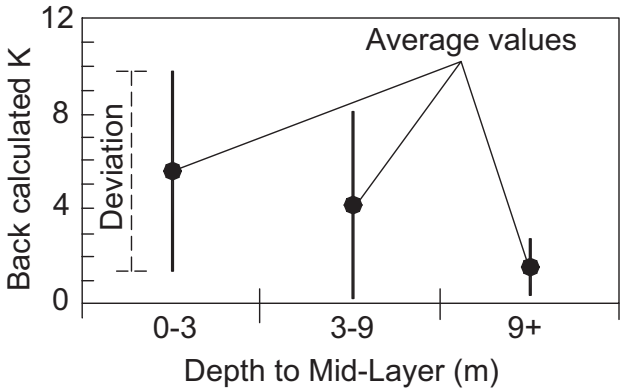

Figure 16. Back-calculated Horizontal stress to Vertical stress ratio, K, vs. Depth to Mid-layer (Harraz, et al., 2005).

Harraz, et al. (2005), evaluated 56 drilled shafts to determine the skin resistance intensity, f_s. The values of f_s derived from field measurements were compared to the values of f_s predicted using different methods. The SPT N-values were provided in almost all of the tests, and these values were correlated to the friction angle of the soils. The soil shaft interface friction angle was assumed to be equal to the friction angle of the soils. The comparisons for sands, sandy gravels, and gravels are shown in Figure 14. The Rollins, et al. (2005), method provides a reasonable prediction for sandy gravels; but the prediction for gravels is still too conservative. The Tomlinson (2001), Kulhawy (1989), Meyerhoff (1976), and Reese and O'Neill (1999) methods under predict the skin resistance for all soil types, especially gravels. To match the predicted values of f_s with the measured values of f_s, the measurement results were used in the back calculation of K values shown in Figure 15 and Figure 16. The trend of variation of K with depth is the same as that observed in the study of Rollins, et al., (2005). The initial empirical model to evaluate K values is shown in Figure 17. This model, shown in Figure 18, gives a better prediction of f_s than any of the other methods mentioned above.

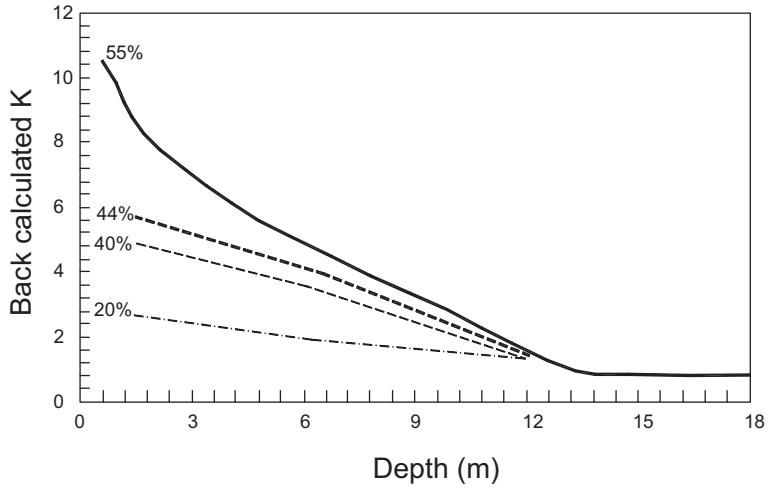

Figure 17. Initial empirical model (Harraz, et al., 2005).

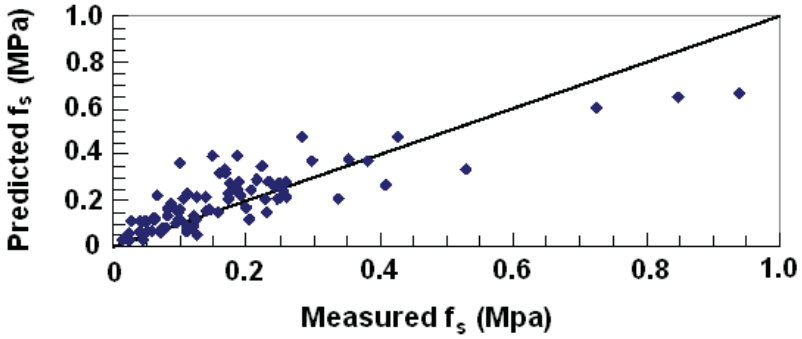

Figure 18. Predicted and actual f_s values for sands, sand gravels, and gravels using the initial empirical model (Harraz, et al., 2005).

2.2.2.2 End bearing in cohesionless soil

According to O'Neill and Reese (1999), tip resistance for cohesionless soil with blow count $N_{SPT} \leq 50$ B/0.3 m can be found by following equation:

$$q = 57.5 N_{SPT} \text{ kPa} \leq 2.9 \text{ MPa} \qquad \text{(Eq. 13)}$$

when $N_{SPT} > 50$ B/0.3 m, q should be calculated according to the equations for intermediate geomaterials (IMGs) (O'Neill and Reese, 1999).

The above-discussed methods are also adopted by the Federal Highway Administration in its drilled design manual (O'Neill and Reese, 1999).

2.3 LOAD TRANSFER CURVES

The effect of anomalies on drilled shaft capacity depends on the anomaly location, size, and load transfer characteristics along the soil shaft interface. The effect of a anomaly occurs at a particular depth where the axial structural capacity is less than the magnitude of the load on the shaft depicted by the load transfer curve at that depth. This will be discussed in more details in Chapter 5. The Winkler concept-based load transfer assumes that the load transfer at a certain depth and at the shaft base is independent of the shaft displacement at other locations (Reese, et al., 2005). The finite element method can more realistically model and analyze the performance of a drilled shaft-soil system, where a drilled shaft is modeled by beam-column elements and soil is modeled by spring elements as shown in Figure 19. The load versus displacement relationship is nonlinear for side (skin) and base resistances as shown in Figure 19. The properties of spring elements are depicted by its soil properties, such as shear modulus, Poisson's ratio, and the strength of its soils.

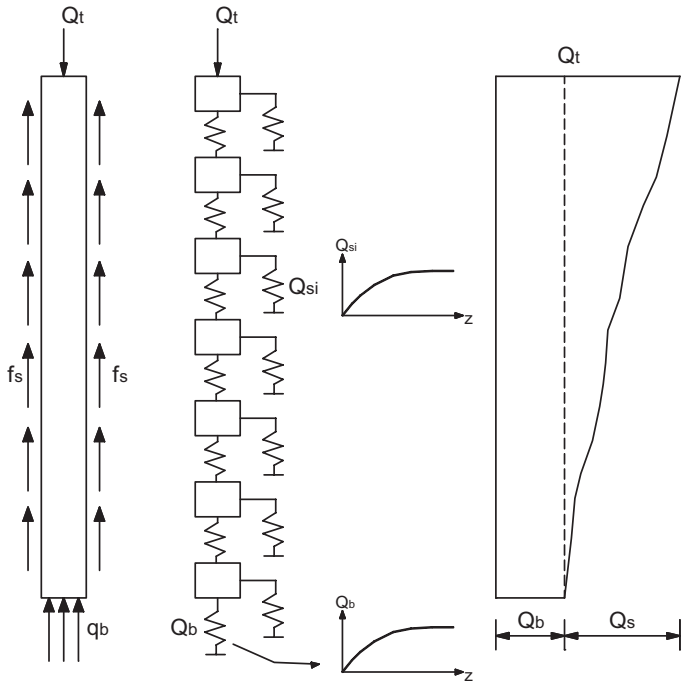

Figure 19. Numerical model of an axially loaded shaft and load transfer curve.

2.3.1 Theoretical load transfer curve

2.3.1.1 Elasto-perfect plastic model

The shear stress (τ) increases linearly with shear strain (γ) at a load smaller than the ultimate load. The relationship becomes perfectly plastic when the ultimate load is reached as shown in Figure 20. The model parameters are shear modulus ($G_{\max}$) and ultimate shear stress (τ_{ult}).

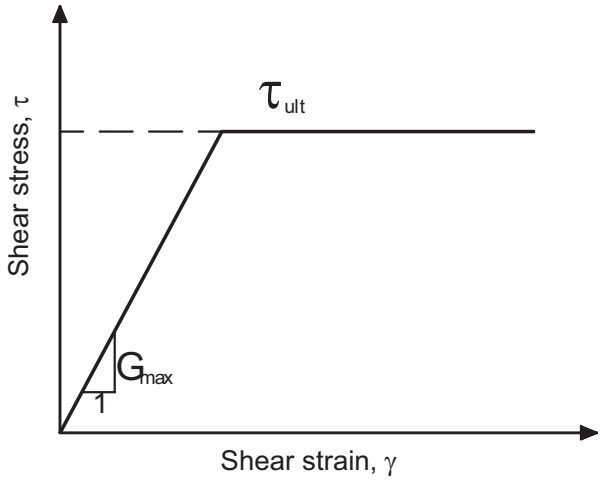

Figure 20. Elasto-perfect plastic model.

2.3.1.2 Hyperbolic model

Duncan and Chang (1970) developed the hyperbolic model to simulate the nonlinear stress-strain behavior of soils. Subsequently, it was also used to model the nonlinear load-settlement relationship of drilled shafts by several researchers, such as Kraft, et al. (1981), and Mosher (1984). The following hyperbolic equation depicts the shear stress versus the shear strain relationship for skin resistance along the perimeter of drilled shafts:

$$\tau = \frac{\gamma}{\frac{1}{G_{\max}} + \frac{\gamma}{\tau_{ult}}} \qquad \text{(Eq. 14)}$$

where

γ = shear strain

$G_{\max}$ = initial shear modulus

τ_{ult} = ultimate shear stress that the hyperbola merges asymptotically

τ = shear stress corresponding to shear strain γ

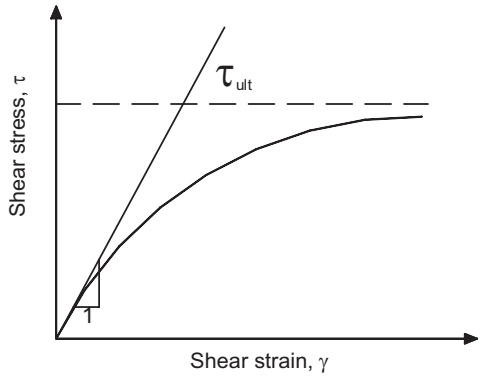

Figure 21. Hyperbolic model.

The tangent shear modulus can be calculated by differentiating Eq. (14):

$$G_t = \frac{\partial \tau}{\partial \gamma} = G_{\max}\left(1 - \frac{\tau}{\tau_{ult}}\right)^2 \qquad \text{(Eq. 15)}$$

The maximum shear stress, $\tau_{\max}$, approaches asymptotically the ultimate shear stress, τ_{ult}, by a factor R_f: $\tau_{\max} = \tau_{ult} R_f$ in which R_f is a constant that varies from 0.75 to 1.0 depending on soil type (Duncan and Chang, 1970), and the failure is reached at a finite strain. Fahey and Carter (1993) proposed another form of hyperbolic model with two curve fitting parameters, f and g, to make it easier to change the shape of the stress strain curve:

$$\frac{G_s}{G_{\max}} = 1 - f\left(\frac{\tau}{\tau_{\max}}\right)^g \qquad \text{(Eq. 16)}$$

where G_s = secant shear modulus

f and g = curve fitting parameters with values ranging from 0 to 1.0.

The shear stress versus shear strain relationship is expressed as Eq. 17:

$$\frac{\tau}{\gamma} = G_{\max}\left[1 - f\left(\frac{\tau}{\tau_{\max}}\right)^g\right] \qquad \text{(Eq. 17)}$$

The tangent shear modulus is given as:

$$G_t = G_{\max}\frac{\left[1 - f\left(\frac{\tau}{\tau_{\max}}\right)^g\right]^2}{\left[1 - f\left(1-g\right)\left(\frac{\tau}{\tau_{\max}}\right)^g\right]} \qquad \text{(Eq. 18)}$$

Figure 22 shows the variation of tangent shear modulus for hyperbolic and modified hyperbolic models. The figure shows that the reduction of tangent shear modulus of a modified hyperbolic model is faster than hyperbolic model at a low ratio of τ and $\tau_{\max}$.

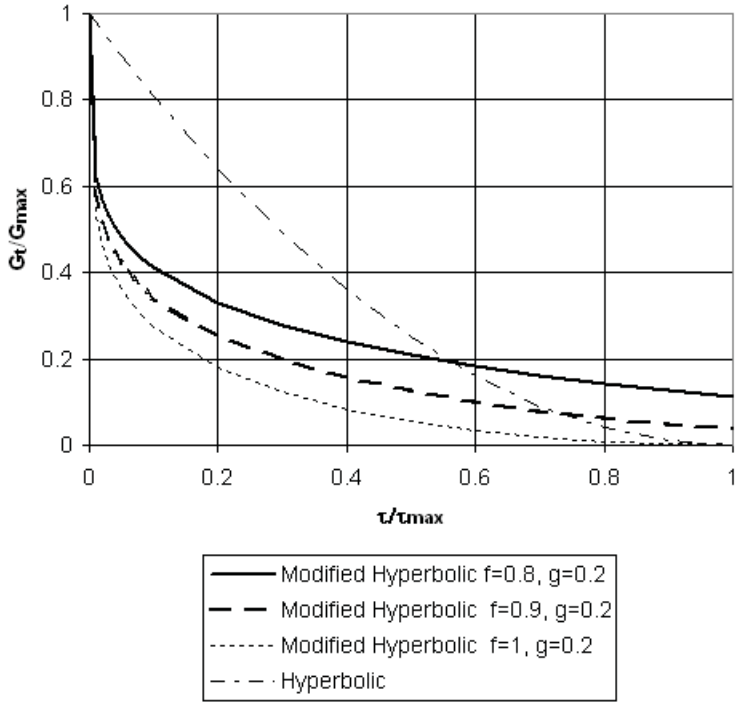

Figure 22. Variation of tangent shear modulus for hyperbolic and modified hyperbolic models.

2.3.1.3 Determination of parameters for nonlinear spring

2.3.1.3.1 Initial shear modulus

The initial shear modulus of a soil, $G_{\max}$, is related to its shear wave velocity, V_s, and mass density, ρ, through the following equation:

$$G_{\max} = \rho V_s^2 \qquad \text{(Eq. 19)}$$

In the laboratory, resonant column tests (Hardin and Drnevich, 1972) were performed to measure the shear wave velocity and formulate the following equation to evaluate the values of $G_{\max}$ at low shear strain:

$$G_{\max}/p_a = 321\frac{(2.97-e)}{1+e}OCR^M\left(\bar{\sigma}_0/p_a\right)^{0.5} \qquad \text{(Eq. 20)}$$

where e is the void ratio (≤ 2); $\bar{\sigma}_0$ is the mean principal effective stress; and the M exponent is related to PI as given in Table 4. p_a is atmospheric pressure, $p_a = 101.4$ kPa.

Table 4. Exponent M for shear modulus (Hardin and Drnevich, 1972)

Plasticity index, PI	Exponent, M
0	0
20	0.18
40	0.30
60	0.41
80	0.48
≥ 100	0.50

2.3.1.3.2 Spring stiffness

The parameters for nonlinear spring can be determined by soil properties such as shear modulus and Poisson's ratio. Randolph and Wroth (1978) derived an expression for stiffness, K_s, of spring using a concentric cylinder approach as shown in Figure 23 with some assumptions:

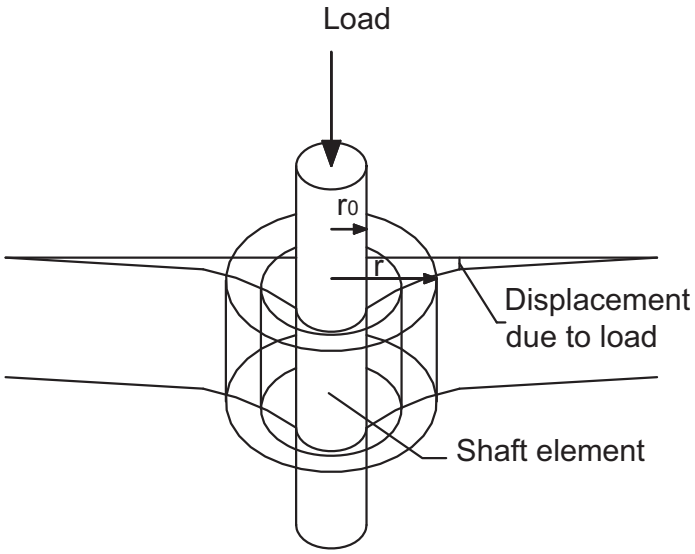

Figure 23. Shearing of concentric cylinders (Kraft, et al., 1981).

- Soil radial displacements are negligible compared to the vertical displacement. Therefore, simple shear conditions prevail.

- Shear stress decreases linearly with the distance from the shaft center such as $\tau = \tau_0 r_0 / r$ where τ is the shear stress at distance r; τ_0 is the shear stress at the shaft soil interface; and r_0 is the shaft radius.

- Shear stress in the soil becomes negligible at the radial distance r_m.

The load-displacement relation can be written as follows:

$$z_s = \tau_0 r_0 \int_{r_0}^{r_m} \frac{dr}{Gr} \qquad \text{(Eq. 21)}$$

where z_s is the shaft element displacement.

For a constant G value, Eq. 21 reduces to:

$$z_s = \frac{\tau_0 r_0}{G} \ln\left(\frac{r_m}{r_0}\right) \quad \text{(Eq. 22)}$$

The spring stiffness is:

$$K_s = \frac{\tau_0}{z_s} = \frac{G}{r_0 \ln\left(\frac{r_m}{r_0}\right)} \quad \text{(Eq. 23)}$$

where r_0 = shaft radius

G = shear modulus

r_m = the radial distance at which the shear stress in the soil becomes negligible. This value for r_m can be estimated by the following equation (Randolph and Wroth, 1979):

$$r_m = 2.5L\rho(1-\nu) \quad \text{(Eq. 24)}$$

where

L = shaft embedment depth

ρ = factor of vertical homogeneity of soil stiffness: $\rho = G_M / G_T$ (G_M is the shear modulus at the shaft mid-depth, and G_T is the shear modulus at the shaft base)

ν = Poisson's ratio of the soil.

Guo and Randolph (1997) proposed a more general form of Eq. (24):

$$r_m = A\frac{1-\nu_s}{1+n}L + Br \quad \text{(Eq. 25)}$$

where A and B are factors depending on shaft geometry, shaft soil stiffness, and various thicknesses of the finite soil layer.

The base stiffness can be approximated using Boussinesq's solution for a rigid footing resting on elastic half-space (Poulos and Davis, 1990):

$$K_b = \frac{4Gr_0}{1-\nu} \quad \text{(Eq. 26)}$$

2.3.1.3.3 Ultimate force

The ultimate force can be calculated by the method shown in the above section. For side resistance of drilled shafts in cohesive soil use:

$$f_{s\max} = \pi D(\alpha c_u) \quad \text{(Eq. 27)}$$

For end bearing resistance of drilled shafts in cohesive soil use:

$$Q_{b\max} = A_p c_u N_c^* \qquad \text{(Eq. 28)}$$

For side resistance of drilled shafts in cohesionless soil use:

$$f_{s\max} = \pi D \beta \sigma'_{vz} \qquad \text{(Eq. 29)}$$

For end bearing resistance of drilled shafts in cohesionless soil use:

$$Q_{b\max} = A_p \sigma'_{vz} N_q \qquad \text{(Eq. 30)}$$

2.3.2 Load transfer curves from field test studies

Empirically-based load transfer curves were proposed to fit the experimental data. Table 5 below summarizes the empirical load transfer function proposed by API (1993) and Vijayvergiya (1977). Figure 24 is the shaft base load versus the shaft base displacement plotted from data given in Table 5 recommended by API (1993). The mobilized bearing capacity, Q, is equal to the ultimate bearing capacity, Q_b, at the shaft base displacement equal to or greater than 0.1 multiplied by the of shaft diameter, D.

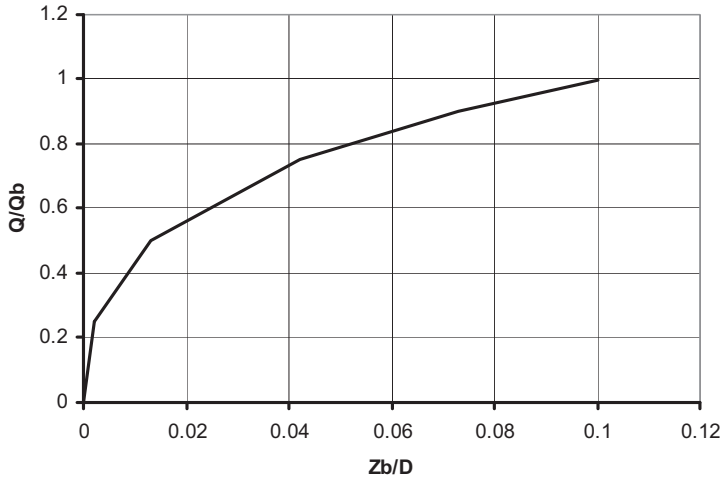

Figure 24. Shaft base load and shaft base displacement curve (API 1993).

O'Neill and Reese (1999) developed the normalized curves for side-shear and end-bearing resistances by evaluating the results of several field load tests of instrumented drilled shafts in cohesive and cohesionless soils as shown in Figure 25 to Figure 28. Rollins, et al. (2005), also represented the normalized load versus displacement curves and compared it to the similar curves developed by O'Neill and Reese (1999) for slightly cemented sands as shown in Figure 29 for gravelly sands and gravels. These curves can be used to determine the load displacement

behavior by using either the elasto-plastic or the hyperbolic model if the ultimate load and the drilled shaft diameter are known.

Table 5. Empirical load transfer curves.

Author	T-Z curve for side spring	$Q_b - Z$ curve for base spring
API (1993)	$\tau_s = \tau_{\max} \frac{z_s}{z_c}$ for $z_s \le z_c$ $\tau_s = \tau_{\max}$ for $z_s > z_c$	Tabulated curve Z_b/D | $Q_b/Q_{b\max}$ 0.0020 | 0.25 0.1300 | 0.50 0.0420 | 0.75 0.0730 | 0.90 0.1000 | 1.00
Vijayvergiya (1977)	$\tau_s = \tau_{\max}\left(2\sqrt{\frac{z_s}{z_c}} - \frac{z_s}{z_c}\right)$ for $(z_s \le z_c)$ $\tau_s = \tau_{\max}$ for $z_s > z_c$	$Q_b = Q_{b\max}\left(\frac{z_b}{z_c}\right)^{\frac{1}{3}}$ for $z_s \le z_c$ $Q_b = Q_{b\max}$ for $z_s > z_c$

where

τ_s = shear stress at soil shaft interface

$\tau_{\max}$ = maximum shear stress at soil shaft interface

z_s = shaft segment displacement

z_c = displacement at failure

z_b = base displacement

Q_b = base resistance

$Q_{b\max}$ = ultimate base resistance

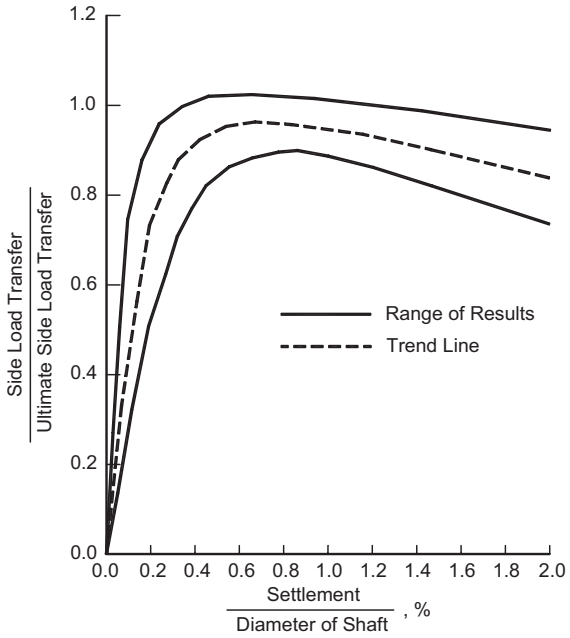

Figure 25. Normalized side load transfer for drilled shafts in cohesive soil (after O'Neill and Reese, 1999).

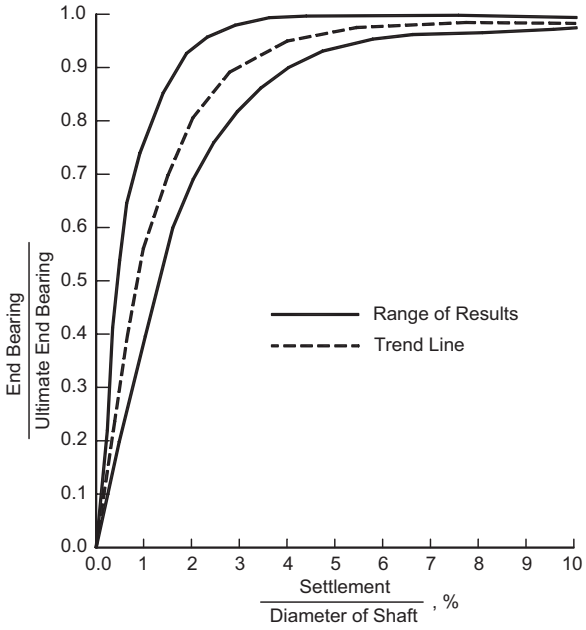

Figure 26. Normalized base load transfer for drilled shafts in cohesive soil (after O'Neill and Reese, 1999).

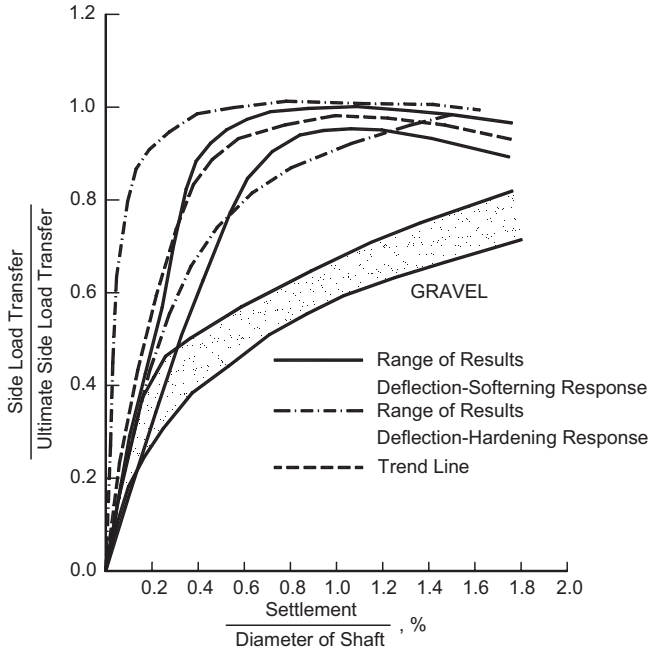

Figure 27. Normalized side load transfer for drilled shafts in cohesionless soil (after O'Neill and Reese, 1999).

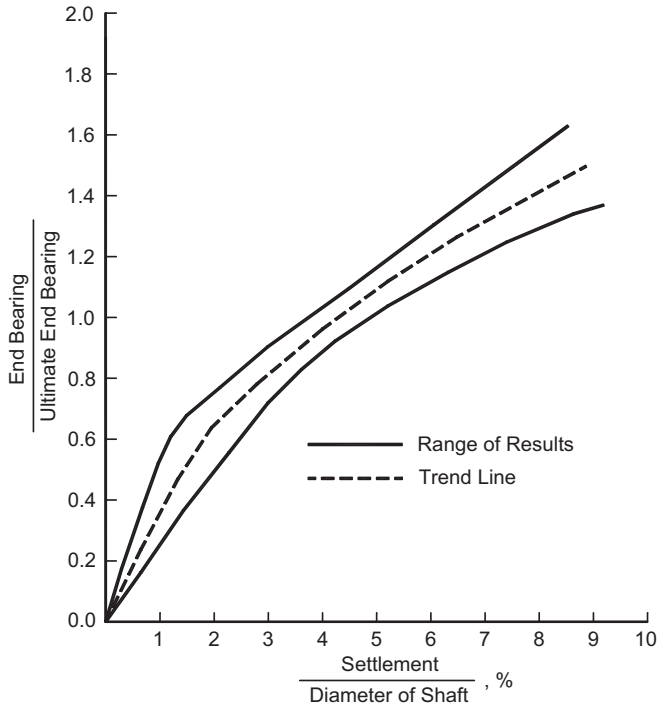

Figure 28. Normalized base load transfer for drilled shafts in cohesionless soil (after O'Neill and Reese, 1999).

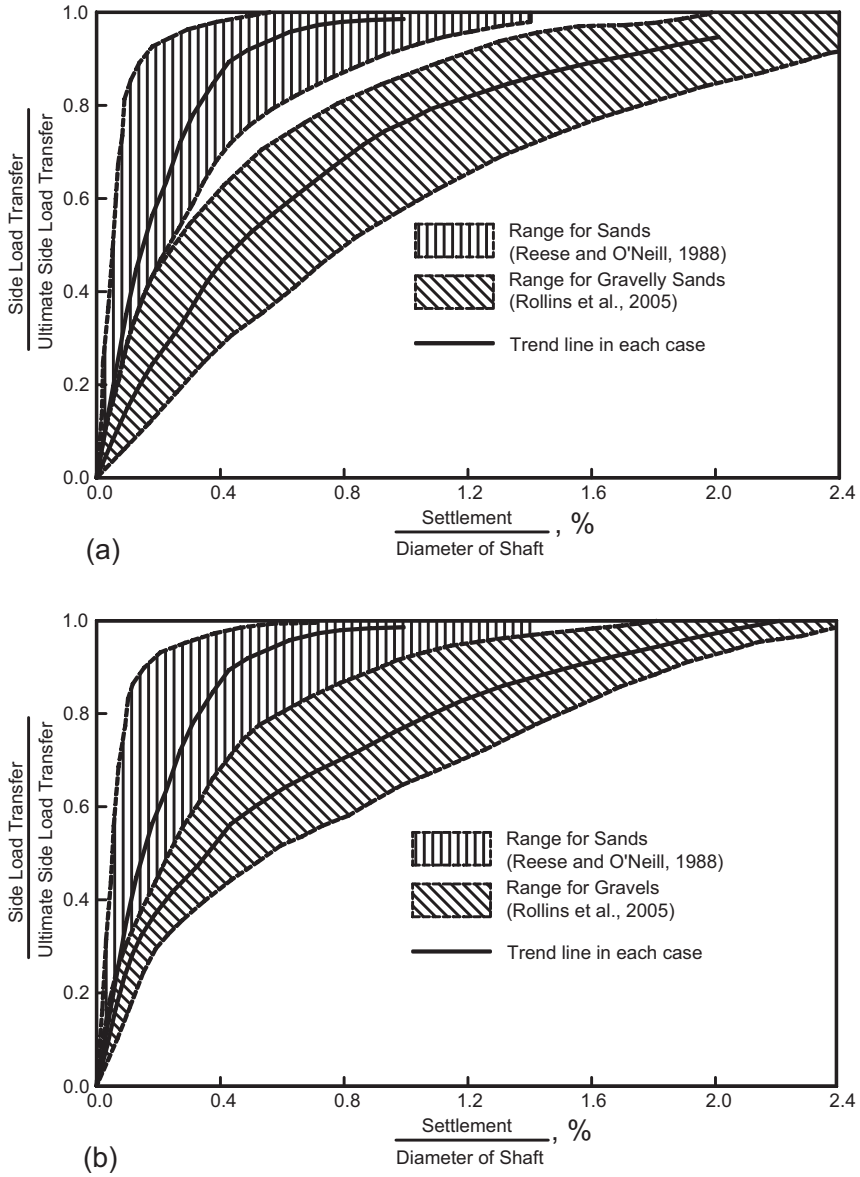

Figure 29. Normalized base load transfer for drilled shafts in cohesionless soil (after Rollins, et al., 2005).